Journal of Catalysis 272 (2010) 1–8

Contents lists available at ScienceDirect

Journal of Catalysis

journal homepage: www.elsevier.com/locate/jcat

Structural features of p-type semiconducting NiO as a co-catalyst for photocatalytic water splitting

Che-Chia Hu, Hsisheng Teng *

Department of Chemical Engineering and Center for Micro/Nano Science and Technology, National Cheng Kung University, Tainan 70101, Taiwan

ARTICLE INFO

Article history:
Received 28 October 2009
Revised 15 March 2010
Accepted 16 March 2010
Available online 24 April 2010

Keywords:
$NaTaO_3$
NiO
Water splitting
Photocatalyst
Co-catalyst

ABSTRACT

Perovskite-like $NaTaO_3$ photocatalysts, synthesized by sol–gel and solid-state methods, were loaded with NiO co-catalyst to enhance water splitting activity under UV illumination. Activity increased significantly with NiO loading and reached a maximum at 3 and 0.7 wt%, respectively, for the sol–gel and solid-state synthesized $NaTaO_3$. Beyond this point, photocatalytic activity decreased with further loading. Analysis using X-ray diffraction, high-resolution transmission electron microscopy, and diffuse reflectance spectroscopy shows that the interdiffusion of Na^+ and Ni^{2+} cations created a solid–solution transition zone on the outer sphere of $NaTaO_3$. For NiO contents less than 3 wt%, no NiO clusters appeared on the $NaTaO_3$ surface, and the reduction/oxidation pretreatment did not enhance photocatalytic activity. The high activity resulting from a low NiO loading suggests that the interdiffusion of cations heavily doped the p-type NiO and n-type $NaTaO_3$, reducing the depletion widths and facilitating charge transfers through the interface barrier.

1. Introduction

In the field of photon energy conversion, photocatalytic water splitting represents a viable technique for producing renewable and clean hydrogen energy using light illumination [1,2]. To date, numerous metal oxide semiconductor materials have been used to catalyze water into H_2 and O_2, e.g., TiO_2 [3–5], $SrTiO_3$ [5], $InTaO_4$ [6], $Sr_2M_2O_7$ (M = Ta, Nb) [7], $H_2La_{2/3}Ta_2O_7$ [8], $K_4Nb_6O_{17}$ [9], and $NaTaO_3$ [10–21]. Among these materials, $NaTaO_3$ has exhibited promising activity and stability under UV irradiation, especially when loaded with co-catalyst. Therefore, $NaTaO_3$ is becoming a model compound for in-depth investigations on a variety of aspects of photocatalytic water splitting [22–24].

Most metal oxides are n-type semiconductors, which create a depleted space charge region when brought into contact with water. Because of the high electric field in the space charge region, photogenerated holes migrate toward the interface while electrons migrate toward the interior. In this case, a co-catalyst, which serves as an electron trap, is needed to assist water reduction for H_2 production [25–28]. Platinum is generally used as a co-catalyst for H_2 generation [3–5]. However, a Schottky barrier typically forms between Pt and metal oxide catalysts. When $NaTaO_3$ is used as a photocatalyst for water splitting, Pt does not provide sites for effective H_2 generation [8]. This may be because the Pt co-catalyst also catalyzes the back reaction between H_2 and O_2 [29–32] or because it does not create a favorable interface for $NaTaO_3$ to facilitate charge transfer. In contrast, NiO loading effectively introduces active sites on $NaTaO_3$ for water splitting [10–14].

NiO is a p-type semiconductor with a band gap energy ranging within 3.5−4.0 eV [33]. When in contact with water, a p-type semiconductor forms a band that is bent to lead photogenerated electrons into the aqueous phase. The p-type conductivity of NiO results from the presence of Ni^{3+} ions and cationic vacancies due to the incorporation of chemisorbed oxygen into the NiO lattice [34–37]. The Ni^{3+} ions are positive holes. Because of the low concentration of Ni^{3+}, NiO has a low conductivity. The conductivity of NiO can be increased by adding an aliovalent dopant. For example, NiO can react with alkaline oxide to form $A_xNi^{2+}_{1-2x}Ni^{3+}_xO$ (A = alkaline metal), which exhibits a conductivity much higher than that of NiO [33]. Therefore, the Na^+ ions in $NaTaO_3$ may help $NaTaO_3$ and NiO construct an effective p/n junction [38,39], which works as an active site for H_2 evolution. However, the structure of NiO as a co-catalyst has never been explored in detail.

On the basis of the discussion above, a detailed examination of the structure of the NiO deposited on a photocatalyst is essential to elucidating the charge transfer mechanism at the water/catalyst interface. Therefore, this study investigates the crystalline framework of the NiO/$NaTaO_3$ interface using the selected area electron diffraction technique. Based on the revealed crystalline structure, this study proposes a band energy diagram for this p-NiO/*n*-$NaTaO_3$ junction in an attempt to illustrate how the NiO co-catalyst can effectively promote the activity of various oxide photocatalysts in water splitting.

* Corresponding author. Fax: +886 6 2344496.
E-mail address: hteng@mail.ncku.edu.tw (H. Teng).

0021-9517/$ - see front matter © 2010 Elsevier Inc. All rights reserved.
doi:10.1016/j.jcat.2010.03.020

2. Experimental

Sol–gel and solid-state methods were used to synthesize $NaTaO_3$ specimens. The sol–gel synthesis method was analogous to those reported elsewhere [17,18]. In brief, solutions of CH_3COO-Na (Nihon Shiyaku, Japan), $TaCl_5$ (Alfa Aesar, USA), and citric acid ($C_6H_8O_7{\cdot}H_2O$; Riedel–de Haën, Germany) were mixed at a Na/Ta/citric acid molar ratio of 1/1/5 to form a sol solution. The solution was continuously stirred at 80 °C until the sol became a coagulated gel. This gel was then calcined at 350 °C for 1 h and then at 500 °C for 3 h to produce the sol–gel synthesized $NaTaO_3$ product, which was designated as SG. $NaTaO_3$ was also synthesized following the conventional solid-state method [17,18], in which a mixture of Na_2CO_3 (Nihon Shiyaku, Japan) and Ta_2O_5 (Alfa Aesar, USA) powders was calcined in air at 1200 °C for 10 h. This calcination was conducted three times with intermediate grinding at ambient temperature. To compensate for volatilization loss, the amount of Na in the precursor mixture was 5% in excess. The resulting solid-state synthesized powder was designated as SS.

To load NiO onto the synthesized $NaTaO_3$ catalysts (SG and SS), 1 g of $NaTaO_3$ powder and a suitable amount of aqueous $Ni(NO_3)_2{\cdot}6H_2O$ (Showa, Japan) solution were mixed in a crucible. The slurry was stirred continuously with a glass rod in a water bath at 80 °C to evaporate the water. The dried mixture was then calcined in air at 350 °C for 1 h to produce a $NiO/NaTaO_3$ catalyst. Previous research indicates that a Ni@NiO core–shell structure is effective as a co-catalyst for water splitting [2,30]. For comparison, some of the prepared $NiO/NaTaO_3$ catalysts were reduced in a H_2 atmosphere at 400 °C for 2 h and subsequently oxidized in air at 200 °C for 1 h to produce catalysts deposited with Ni@NiO compounds, i.e., $NiO_x/NaTaO_3$ catalysts.

The crystalline structure of the specimens was characterized by powder X-ray diffraction (XRD) using a diffractometer (Rigaku RINT 2100, Japan) with Cu Kα radiation ($\lambda = 1.5418$ Å) at 40 kV and 40 mA. The XRD patterns were collected at 2θ angles of 20–70° at a scan rate of 4 deg min^{-1}. The surface morphologies and microstructures were explored with scanning electron microscopy (SEM; JEOL JSM-6700F, Japan) and high-resolution transmission electron microscopy (HRTEM; FEI Tecnai, G2 F20, Philips, USA). The N_2 surface area was determined with the Brunauer–Emmet–Teller (BET) equation at −196 °C using an adsorption apparatus (Micromeritics ASAP 2010, USA). Diffuse reflection spectra were measured for the specimens using an ultraviolet–visible–near infrared (UV–Vis–NIR) spectrometer (Hitachi U-4100, Japan) equipped with an integration sphere.

Photocatalytic reactions were conducted at ca. 25 °C in a gas-closed inner irradiation system. The light source was a 400-W high-pressure mercury lamp (SEN HL400EH-5, Japan). One gram of the $NaTaO_3$ powder was suspended in 1100 ml of pure water by a magnetic stirrer in an inner irradiation cell made of quartz. A jacket between the mercury lamp and the reaction chamber was filled with flowing thermostatted cooling water. The mercury lamp spectrum with which the reacting system was irradiated was obtained using a photodetector (Oriel, Model 71964, USA) coupled with a Cornerstone 130 monochromator (Oriel) having a bandwidth of 10 nm. The amounts of H_2 and O_2 evolved were determined using gas chromatography (Hewlett–Packard 6890, USA; molecular sieve 5A column, thermal conductivity detector, argon carrier gas).

3. Results and discussion

Fig. 1 shows the SEM images of naked SG and SS $NaTaO_3$ powders. The particle size of the SS $NaTaO_3$ was primarily within 13 μm, as Fig. 1a indicates. Fig. 1b shows that the sol–gel method synthesized a powder (SG) with particles smaller than those of SS. In addition, the surface of SS was smooth, in contrast to the rugged surface of SG. Because both particle size and surface roughness affect the exposed area of the specimens, Table 1 shows that the naked SG $NaTaO_3$ had a surface area of 28 $m^2\ g^{-1}$, much greater than that of the SS $NaTaO_3$.

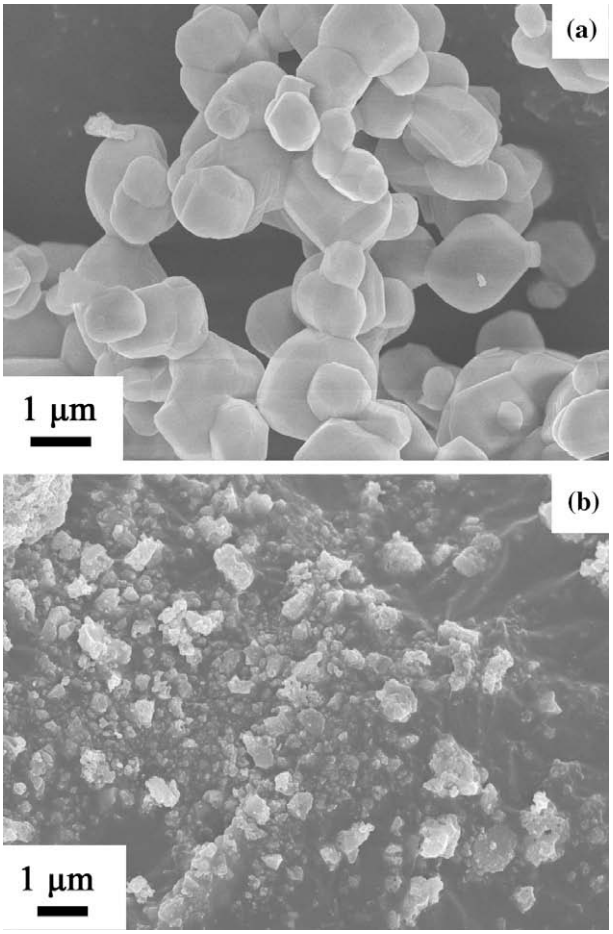

Fig. 1. SEM images of naked $NaTaO_3$ powders: (a) the solid-state synthesized $NaTaO_3$, i.e., SS; (b) the sol–gel synthesized $NaTaO_3$, i.e., SG.

NiO loading varied the surface roughness of these $NaTaO_3$ powders. Table 1 shows that the surface area of NiO/SS increased with increasing NiO content, as well as with an increase in surface roughness. Conversely, the surface area of the NiO/SG specimens decreased with NiO loading up to 8 wt%. The loaded NiO may have filled the voids on the SG $NaTaO_3$, leading to a decrease in surface area. The greater surface area of the 15 wt% NiO/SG, relative to that of 8 wt% NiO/SG, seems to indicate that extra NiO loading increased surface roughness.

Table 1
The BET surface areas of sol–gel and solid-state synthesized $NaTaO_3$ (SG and SS, respectively) with different amounts of NiO loading.

NiO content in $NaTaO_3$ (wt%)	BET surface area[a] ($m^2\ g^{-1}$)	
	NiO/SG	NiO/SS
0	29	0.6
0.05	29	1.5
0.7	27	1.6
3	24	3.6
8	20	6.8
15	25	10

[a] Surface area of bulk NiO = 30 $m^2\ g^{-1}$.

Fig. 2 shows the XRD patterns of the naked and NiO-loaded $NaTaO_3$ specimens. All specimens exhibited the distinct and sharp diffraction peaks characteristic of $NaTaO_3$. The NiO diffraction peaks are only apparent for specimens with a high NiO loading (>8 wt%). This indicates that the NiO was evenly dispersed on the $NaTaO_3$ surface. Although the $NaTaO_3$ peaks of SG and SS are located at similar positions, our previous studies have identified the crystal structures of SG and SS as monoclinic and orthorhombic, respectively [17,18,40].

Stoichiometric nickel(II) oxide is a pale green solid of very low conductivity. Alkaline metal oxides can react with nickel oxide to form solid solutions and transform insulating NiO to semiconducting $A_xNi^{2+}_{1-2x}Ni^{3+}_xO$ [33]. The introduction of alkaline metal ions stabilizes the p-type conductivity of nickel oxide and turns it black. This study shows that the color of the naked SG and SS was white and that they turned gray with low degrees of NiO loading (<3 wt%). This indicates the presence of black semiconducting nickel oxide in the NiO/$NaTaO_3$ specimens. The Na^+ cations might have penetrated the framework of the deposited NiO to form a solid solution. Crystal type analysis shows that both NiO (with a rock salt structure) and $NaTaO_3$ (with a perovskite-like structure) have cubic close-packing arrays (composed of O and Na/O, respectively) with octahedral sites fully or partially occupied by cations (Ni and Ta, respectively). This structural similarity suggests the partial dissolution of NiO into $NaTaO_3$. Previous research shows that Ni cations can diffuse into Ta_2O_5 easily via thermal treatment because of the similar cationic radii [41], 0.69 and 0.64 Å for Ni and Ta, respectively.

A detailed review of the XRD patterns and the results in this study shows that the 2θ positions of $NaTaO_3$ peaks shift slightly toward a larger 2θ value with NiO loading. For example, the insets of Fig. 2 show the position change of the peak located at ca. 22.8°. The shift toward a larger 2θ value corresponds to contraction of the $NaTaO_3$ perovskite lattice as a result of structural distortion or the replacement of some Na cations (1.02 Å) with smaller Ni cations. The NiO/SG specimens show a more obvious shift in the diffraction peak than the NiO/SS. This is due to the larger surface area of the SG powder, whereby the dissolution of NiO into $NaTaO_3$ is more significant for NiO/SG than for NiO/SS.

Fig. 3 shows the representative HRTEM images and corresponding selected area electron diffraction (SAED) patterns of the NiO/SG catalysts. Fig. 3a shows the naked SG $NaTaO_3$ particles, in which the lattice fringes are visible. The interplanar spacing shown in this figure is approximately 0.2754 nm, which corresponds to the *d*-spacing of (1 0 1) planes in the monoclinic phase $NaTaO_3$ (*P2/m*, JCPDS 74-2485). The inset of Fig. 3a shows the SAED pattern, which matches well the monoclinic $NaTaO_3$ crystal projected along its [0 1 0] direction. For SG powder with NiO content of 0.7 and 3 wt%, HRTEM images (Fig. 3b and c) reveal no NiO clusters. However, the dissolution of NiO into $NaTaO_3$ obviously occurred. NiO loading caused variations in the lattice fringes and electron diffraction patterns around the periphery of the particles. For the 3 wt% NiO/SG catalyst, the inset of Fig. 3c shows that a thin layer of heterostructure was present around the particle periphery, with its lattice fringes deviating from those of SG. To get a better perspective on the structure variation, this study uses selected area elec-

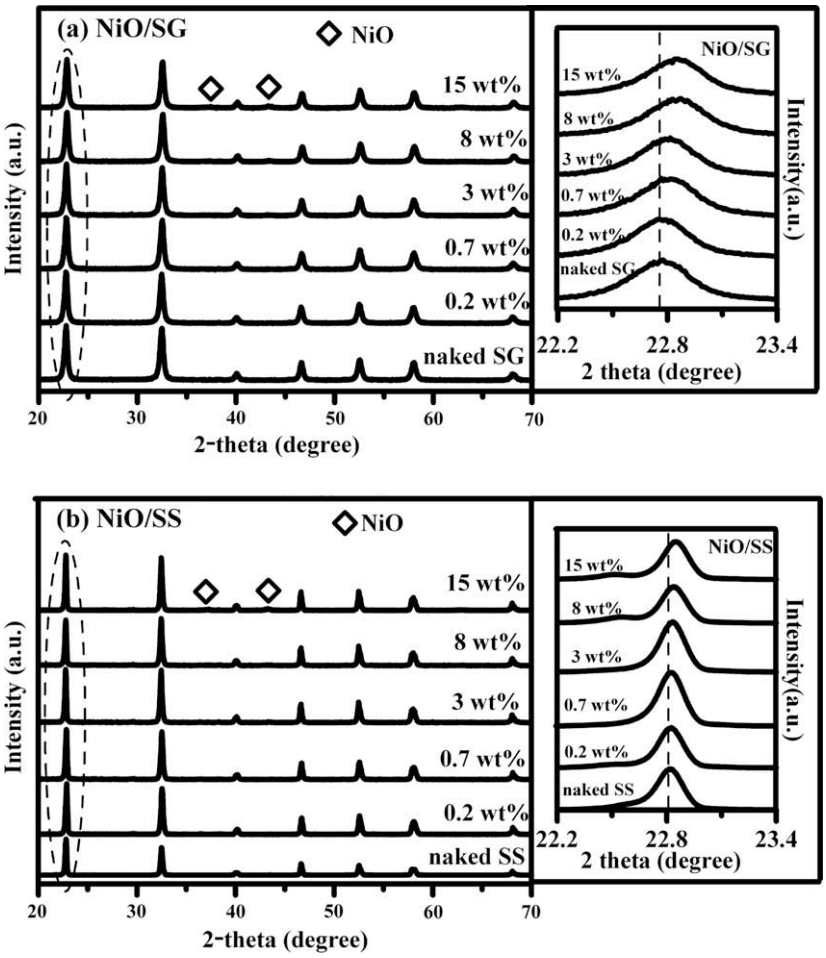

Fig. 2. X-ray diffraction patterns of sol–gel and solid-state synthesized $NaTaO_3$ catalysts with different amounts of NiO loading: (a) NiO/SG catalysts; (b) NiO/SS catalysts. The NiO contents are shown in wt%. The insets show the magnification of the diffraction peak around 22.8°.

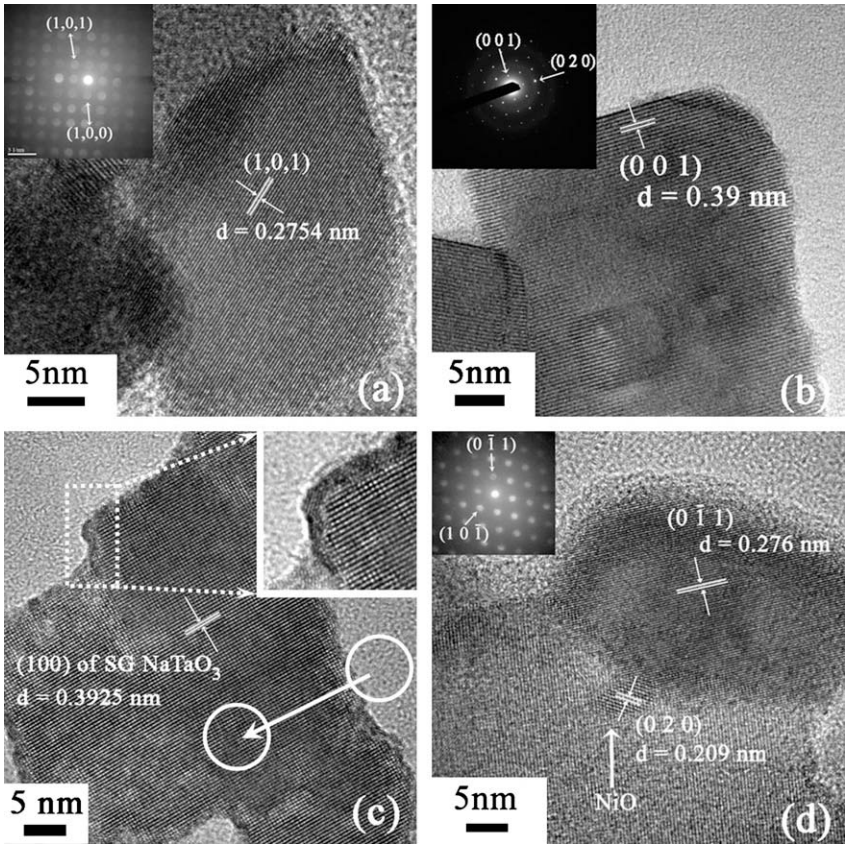

Fig. 3. High-resolution TEM images of SG $NaTaO_3$ catalysts with different amounts of NiO loading: (a) naked SG; (b) 0.7 wt% NiO/SG; (c) 3 wt% NiO/SG; (d) 15 wt% NiO/SG. The insets of (a), (b), and (d) show the selected area electron diffraction patterns of $NaTaO_3$. The inset of (c) shows the magnification of the particle periphery. The arrow in (c) indicates the spots where electron diffraction analysis was conducted; see Fig. 4 for the results.

tron nanobeam diffraction (SAENBD) analysis of the catalyst from the outer sphere of influence to the interior along the direction indicated by the arrow in Fig. 3c.

Fig. 4a–c sequentially shows the SAENBD results from the outer sphere to the interior. The diffraction spots in the outer sphere (Fig. 4a) are not clear. A close inspection reveals that the pattern consists of distorted cubic NiO and distorted monoclinic $NaTaO_3$ crystals. The *d*-spacing of NiO (1 1 1) planes in the pattern is 0.2552 nm, which is significantly greater than the standard value of 0.2441 nm (*Fm3m*, JCPDS 75-0269). This indicates the diffusion of Na^+ into the NiO framework to form a Na/O close packing array, which in turn creates repulsion between the Na and Ni cations to increase the *d*-spacing [42,43]. On the other hand, because of NiO dissolution, the (1 0 0) *d*-spacing of $NaTaO_3$ decreases to a lower value of 0.3892 nm compared to the standard value of 0.3923 nm (*P2/m*, JCPDS 74-2485). For the SAENBD taken from a region slightly inside the outer sphere (Fig. 4b), the monoclinic $NaTaO_3$ pattern (d_{100} = 0.3923 nm) is clearly apparent, accompanied by a highly distorted NiO pattern with a (1 1 1) *d*-spacing of 0.2567 nm. For the SAENBD taken at the interior of the catalyst, Fig. 4c shows that the pattern completely conforms to that of standard monoclinic $NaTaO_3$. This SAENBD analysis shows that the *d*-spacing of $NaTaO_3$ decreases due to NiO dissolution into the framework. This is in good agreement with the XRD results in Fig. 2a. The images in Fig. 3c and the patterns in Fig. 4 demonstrate that for the 3 wt% NiO/SG catalyst, the outer sphere of influence is in fact a transition zone

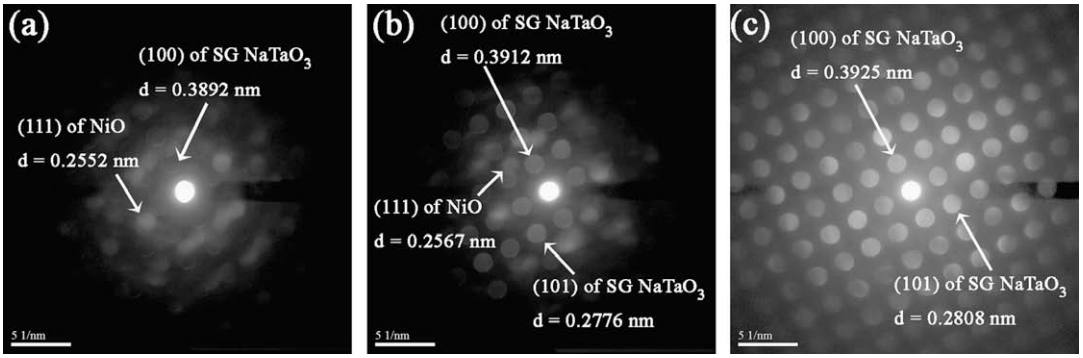

Fig. 4. Selected area electron diffraction patterns of the 3 wt% NiO/SG catalyst obtained sequentially from the outer sphere to the interior, i.e., (a–c) in sequence, along the arrow indicated in Fig. 3c.

characterized by an Ni (or Na) concentration gradient. With a NiO content of 15 wt%, NiO clusters are visible on the SG surface, as shown by the HRTEM image in Fig. 3d. The lattice fringes of the observed cluster show a *d*-spacing of 0.209 nm, which correspond to that of the (0 2 0) planes in the cubic phase NiO.

For the NiO/SS catalysts, NiO clusters are visible at an NiO content as low as 3 wt%. The small surface area of SS is likely responsible for the agglomeration of NiO at this low content. Fig. 5a shows the HRTEM images of the 15 wt% NiO/SS catalyst, clearly showing NiO particles. Fig. 5b–f sequentially shows the SAED analysis conducted from the NiO to the SS interior, as indicated by the arrow in Fig. 5a. The (0 2 2) *d*-spacing of NiO on the catalyst increases when the SAED is taken from NiO toward the catalyst interior. The SAED pattern of SS (Fig. 5f) matches well the orthorhombic $NaTaO_3$ crystal (*Pcmn*, JCPDS 73-0878). The (1 0 1) spacing of orthorhombic $NaTaO_3$ shows a decreasing trend when the analysis is taken from the catalyst interior toward the NiO cluster. This indicates that, similarly to the NiO/SG catalysts, there is a transition zone between the exterior and interior of the NiO/SS catalysts, and this zone has a Ni (or Na) gradient.

This study also presents diffuse reflectance UV–Vis spectroscopic analysis for the NiO/SG and NiO/SS catalysts. Fig. 6 shows the absorbance spectra converted from reflection by the Kubelka–Munk method [44]. The absorption edges of the naked SG and SS were similar, with values of 309 and 302 nm (4.0 and 4.1 eV), respectively. NiO loading resulted in a red shift of the absorption edge and this shift increased with the amount of NiO. Fig. 6 shows that with 15 wt% NiO loading, the absorption band edge shifted to 377 and 390 nm (3.29 and 3.18 eV) for SG and SS, respectively. Bulk NiO has an absorption edge at ca. 3.1 eV (400 nm) and a strong absorption tail in the visible light regime. The latter is associated with *dd* transitions within individual Ni^{2+} ions and gives NiO a pale green color [33]. Fig. 6 shows that the absorbance spectra of $NaTaO_3$ and NiO are different and that the $NiO/NaTaO_3$ catalysts gave an absorbance spectrum intermediate between those of NiO and $NaTaO_3$. This indicates that solid solutions of NiO and $NaTaO_3$ formed on the catalyst surface and agrees with the preceding conclusions drawn by XRD and TEM analyses. In addition, increased NiO loading intensified the gray color of the $NiO/NaTaO_3$ catalysts, reflecting again the penetration of Na^+ into NiO to form stabilized p-type $Na_xNi^{2+}_{1-2x}Ni^{3+}_xO$ solutions. The

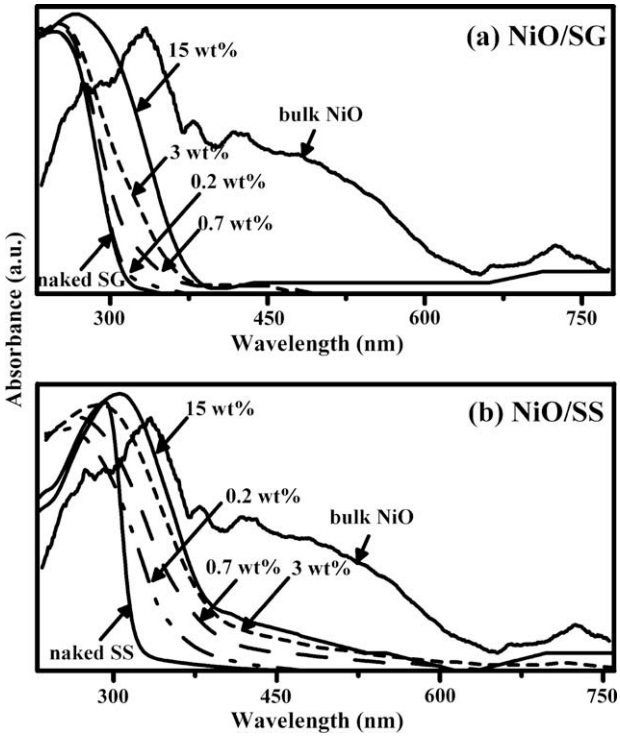

Fig. 6. Diffuse reflectance spectra of the $NaTaO_3$ catalysts with different amounts of NiO loading: (a) the NiO/SG catalysts; (b) the NiO/SS catalysts. The NiO spectrum is provided for comparison.

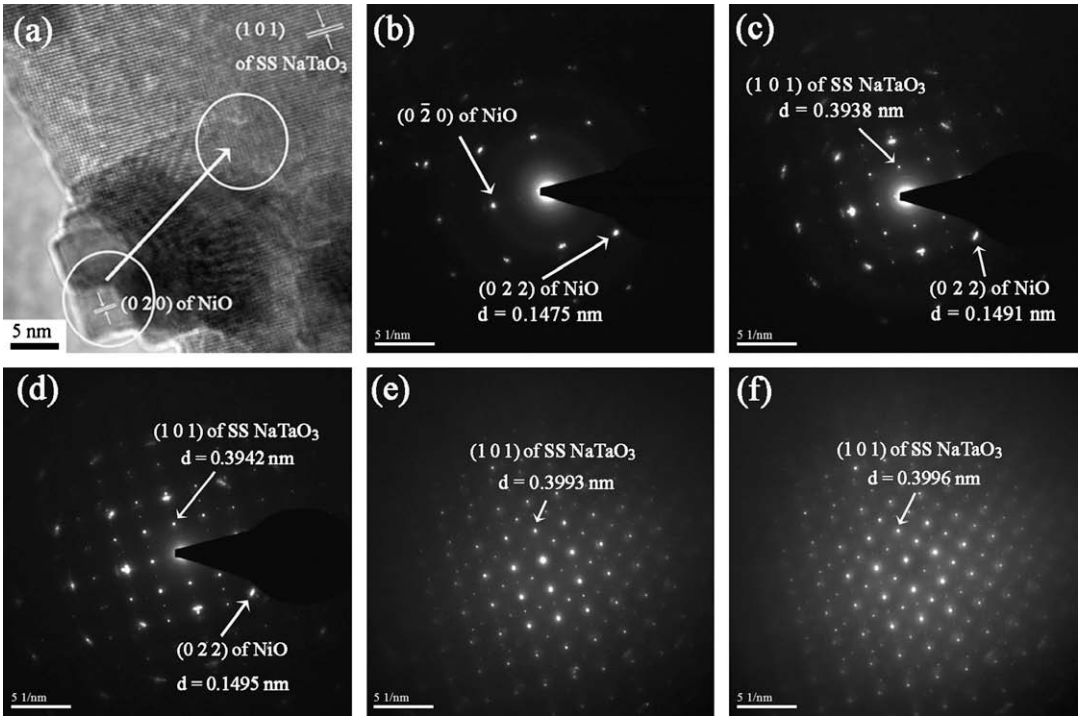

Fig. 5. High-resolution TEM image (a) and selected area electron diffraction patterns (b–f) of the 15 wt% NiO/SS catalyst. (b–f) Sequentially show the electron diffraction patterns obtained from the NiO cluster to the catalyst interior along the arrow indicated in (a).

lack of the absorption tail in the visible light regime for the NiO/SG catalysts can be attributed to a higher degree of NiO dissolution into the SG $NaTaO_3$ (due to higher surface area) than into the SS.

Fig. 7a and b show the evolution of H_2 from photocatalytic reactions of the NiO/SG and NiO/SS catalysts illuminated with a mercury lamp. In principle, H_2 and O_2 were steadily evolved in a stoichiometric ratio of 2:1. In agreement with our previous studies [17,18], the naked SG catalyst exhibited a much higher activity than the naked SS due to differences in electronic characteristics and particle size. After NiO loading, the activity of both the SS and the SG catalysts increased significantly, indicating that the co-catalyst NiO provided an efficient medium for H_2 evolution. Photocatalytic activity increased with the NiO content to its maximum and then decreased with further increases in NiO loading. Fig. 7c summarizes the mean rates of the H_2 and O_2 evolutions using the $NaTaO_3$ catalysts with different NiO contents. The NiO/SG catalysts exhibited a maximum H_2 evolution rate of 9000 μmol h^{-1} g^{-1} at 3 wt% NiO loading, while the NiO/SS catalysts produced a maximum H_2 rate of 147 μmol h^{-1} g^{-1} at 0.7 wt% NiO. Clearly, the SG $NaTaO_3$ has a greater surface area than SS for dispersing NiO. Note that the highest reaction rates occurred when NiO dissolved into $NaTaO_3$, and no NiO cluster was observed by HRTEM. This suggests that the solid solution present in the transition zone (Fig. 3c) and not NiO aggregates serves as the active site for H_2 evolution.

The present study calculated the radiant flux for light with wavelengths less than 310 nm, which corresponds to the absorption edge of $NaTaO_3$. The mercury lamp gave an average flux of 0.15 W cm^{-2} and a total power of 115 W reaching the reacting system. In combination with the obtained irradiation spectrum, the calculation showed that the mercury lamp irradiated the reacting system at an incident photon rate of 284 mmol h^{-1}. The apparent quantum yield for H_2 evolution (Fig. 7c) was calculated using the following equation:

$$\text{Quantum yield } (\%) = [(\text{number of } H_2 \text{ molecules evolved} \times 2)/(\text{number of incident photons})] \times 100.$$

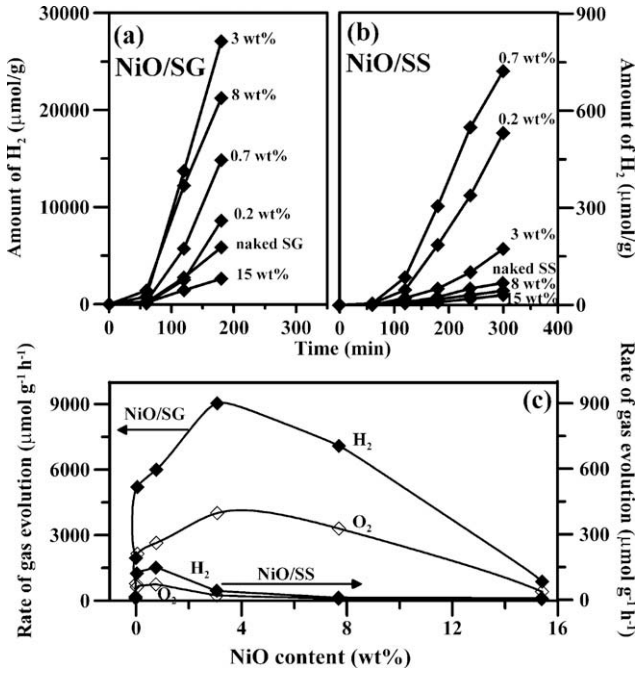

Fig. 7. Timeline of photocatalytic H_2 evolution from 1100 ml pure water suspended with 1 g of the NiO/SG and NiO/SS catalysts (a and b); the dependence of the H_2 and O_2 evolution rates on NiO content for the NiO/SG and NiO/SS catalysts (c).

Based on the above calculation, the 3 wt% NiO/SG catalyst, which exhibited the greatest H_2 evolution, had an apparent quantum yield of 6.4%.

The influence of co-catalysts on light-driven reactions depends on the type of heterojunction formed at the semiconductor interface. Fig. 8a shows the schematic energy-level diagrams of NiO and $NaTaO_3$ before joining. When NiO and $NaTaO_3$ are brought into contact, their Fermi levels align, due to the charge transfer phenomenon. In an n-type semiconductor ($NaTaO_3$), a depletion region forms near the junction, as Fig. 8b shows. Therefore, under illumination, the n-type $NaTaO_3$ produces a forward-bias voltage that causes electron diffusion across the depletion region to the p-type NiO for H_2 evolution (Fig. 8c).

To activate charge transfer across the junction at the catalyst interface, the NiO co-catalyst is generally pretreated with H_2 reduction and subsequent O_2 oxidation to produce the NiO/Ni double layer structure depicted in Fig. 9 [39]. The work functions of Ni metal and NiO are 5.2 and 4.6 eV, respectively [45]. The alignment of the Fermi levels after joining forms an ohmic-type contact at the NiO/Ni interface, enabling easy charge flow across the junction. On the other hand, the Ni/$NaTaO_3$ contact interface forms a Schottky-

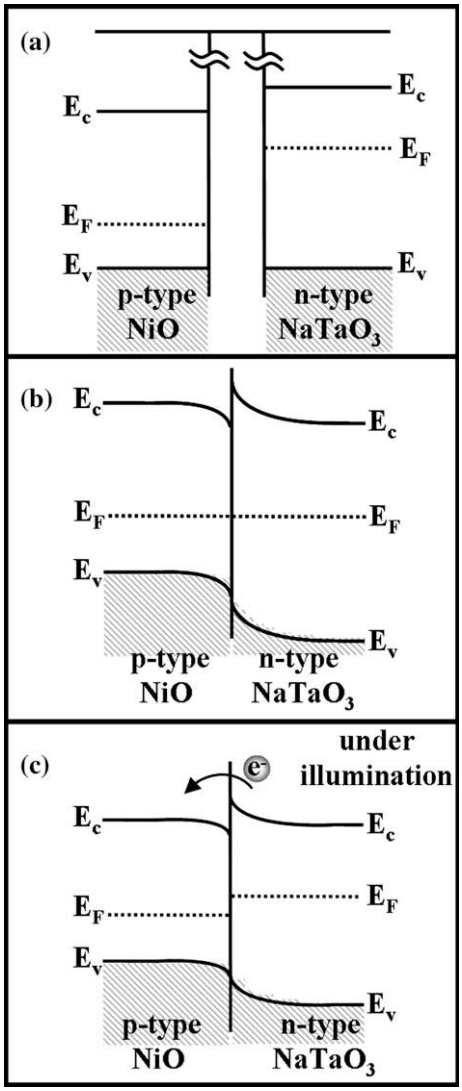

Fig. 8. Schematic energy-level diagrams of NiO and $NaTaO_3$: (a) before joining; (b) after joining; (c) under illumination after joining. E_c, E_v, and E_F represent the energy positions of the conduction band edge, valence band edge, and Fermi level, respectively.

type barrier, with electrons accumulating on the metal side. Under illumination, these electrons are consumed to generate H_2. To replenish electron consumption for the electronic dynamic balance of the Schottky barrier, photogenerated electrons are continuously injected from the bulk of the $NaTaO_3$ toward the metal [46,47]. This is why the formation of a NiO/Ni double layer structure is beneficial for H_2 generation. In an attempt to further promote photocatalytic activity, this study also conducted the reduction/oxidation pretreatment on the NiO/SG catalysts.

Fig. 10 illustrates the performance of the pretreated NiO/SG catalysts, which are designated as NiO_x/SG, under mercury lamp illumination. However, this pretreatment did not improve the photocatalytic activity of NiO/SG except for the one with the highest NiO content (15 wt%). The TEM image in Fig. 3d shows that NiO aggregates are visible on the surface of the SG $NaTaO_3$. This suggests that the reduction/oxidation pretreatment is effective only for catalysts containing NiO aggregates, as it transforms them into a NiO/Ni double layer structure. On the other hand, the NiO/SG catalysts with lower NiO contents (e.g., 3 wt%) were passivated by this treatment. These catalysts had a high photocatalytic activity. The solid solution forming on the outer sphere of influence must have played an important role in promoting photocatalytic activity.

The results in Fig. 4 demonstrate the interdiffusion of Ni^{2+} and Na^+ at the NiO and $NaTaO_3$ interface, forming solid solutions. Doping with cations of valence higher than that of the parent cations may increase the charge concentration and shift the Fermi energy level upward. The opposite is also true for doping with lower valence cations [48]. Therefore, the interdiffusion of Ni^{2+} and Na^+ can form p-doped NiO (i.e., $Na_xNi^{2+}_{1-2x}Ni^{3+}_xO$) and n-doped $NaTaO_3$ (i.e., $Ni_xNa_{1-x}TaO_3$) at the interface. Fig. 11 shows that the depletion layers on both sides of the semiconductors become steeper and reduce their widths because of the doping. This allows charge carriers to tunnel through the barrier. In fact, a practical method for forming ohmic contacts is to heavily dope the semiconductor in the contact region [49,50]. The thickness of the doped layers should depend on the solubility of Ni into $NaTaO_3$ and/or Na into NiO. NiO clusters form on the catalyst surface when the loading amount is above the solubility limit. Based on the investigation with HRTEM (Fig. 3c), the thickness of the p-doped NiO layer is less than 2 nm. Such a low thickness cannot complete the band bending. However, low thickness is beneficial for effective transfer of the photogenerated electrons to the liquid phase for water splitting.

Fig. 11 also illustrates how the solid solution layers can effectively facilitate charge transfer across the NiO/$NaTaO_3$ interface for H_2 generation. Reduction/oxidation pretreatment simply collapses this structural feature, deactivating the catalysts (see the comparison between Figs. 7c and 10). Further, note that a homojunction between the n-doped $NaTaO_3$ and pristine $NaTaO_3$ is present in the interior of $NaTaO_3$ even though the junction is vaguely outlined due to the gradual decrease in Na concentration toward the catalyst interior. Fig. 11 shows that to align the Fermi levels

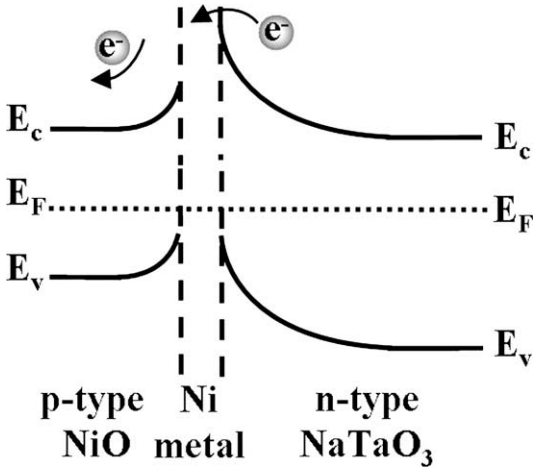

Fig. 9. Schematic energy-level diagrams of NiO_x/$NaTaO_3$ interface. An ohmic type contact formed at the p-NiO/Ni interface, while the Ni/*n*-$NaTaO_3$ contact interface formed a Schottky-type barrier with electrons accumulating on the metal side. E_c, E_v, and E_F represent the energy positions of the conduction band edge, valence band edge, and Fermi level, respectively.

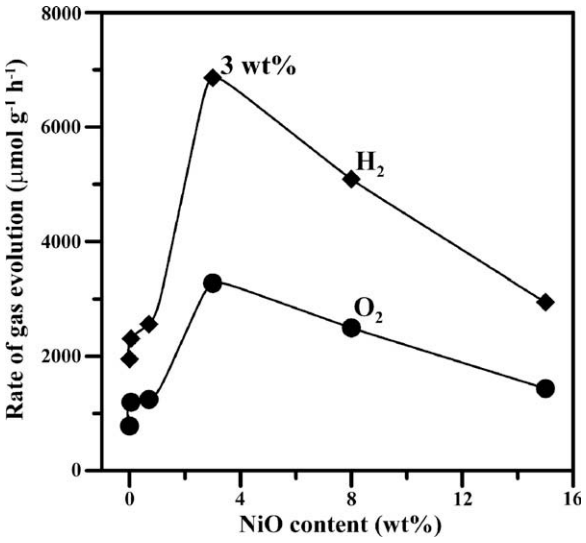

Fig. 10. The dependence of H_2 and O_2 evolution rates on NiO content for the reduction/oxidation pretreated NiO/SG catalysts (i.e., the NiO_x/SG catalysts).

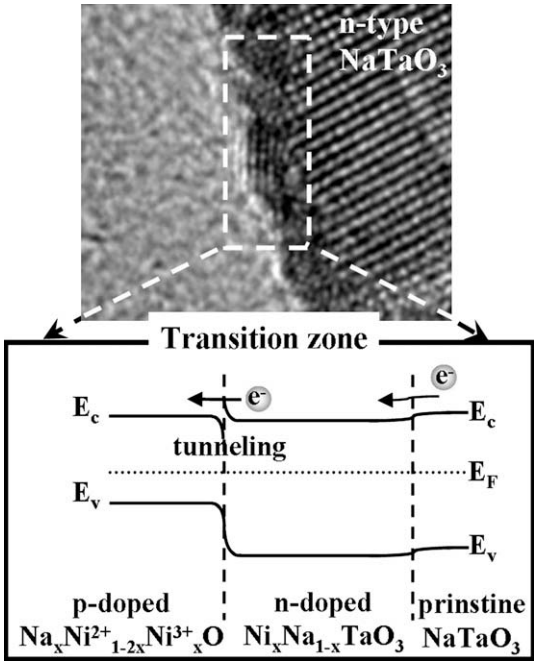

Fig. 11. Schematic energy-level diagrams of the NiO and $NaTaO_3$ contact with interdiffusion of Ni^{2+} and Na^+ to form p-doped NiO (i.e., $Na_xNi^{2+}_{1-2x}Ni^{3+}_xO$) and n-doped $NaTaO_3$ (i.e., $Ni_xNa_{1-x}TaO_3$) at the interface. Steeper band bending and reduced depletion widths appeared at the heterojunction interface. E_c, E_v, and E_F represent the energy positions of the conduction band edge, valence band edge, and Fermi level, respectively.

of the n-doped $NaTaO_3$ and pristine $NaTaO_3$, the conduction bands must be bent to become favorable for transferring the photogenerated electrons from the interior to the exterior sphere. This n-doping role of Ni^{2+} cations explains why the activity of $NaTaO_3$ can be significantly promoted even with a very small amount of NiO loading (0.05 wt%). The improved charge transfer must have made up for the detrimental effect caused by heteroatom doping, which leads to crystal distortion [51–53].

4. Conclusions

Based on HRTEM and electron diffraction analysis, this study demonstrates that depositing the p-type co-catalyst NiO on n-type $NaTaO_3$ forms a solid–solution transition zone at the interface between NiO and $NaTaO_3$ due to the interdiffusion of Ni^{2+} and Na^+ cations. TEM analysis does not show any NiO clusters present on the $NaTaO_3$ surface at NiO content of less than 3 wt%. XRD analysis also shows that this cation interdiffusion caused variations in the crystal structure. Because the valences of the cations are different, the interdiffusion led to p- and n-doping on NiO and $NaTaO_3$, respectively. This heavy doping at the interface may have reduced the depletion widths of NiO and $NaTaO_3$, allowing charge tunneling through the interface barrier. As a result, the photocatalytic activity of $NaTaO_3$ was tremendously enhanced by an NiO loading as low as 0.05 wt%. An interior homojunction between the n-doped $NaTaO_3$ and pristine $NaTaO_3$ caused favorable band bending, which may also play a role in this activity enhancement.

The reduction/oxidation pretreatment of NiO to form an Ni@NiO double layer that enhances water splitting was only applicable for catalysts with NiO clusters on the $NaTaO_3$ surface (i.e., those with high NiO contents). On the other hand, this pretreatment was detrimental to the activity of the $NiO/NaTaO_3$ catalysts with low NiO content. This result partially explains the formation of the solid solutions, which are resistant to NiO_x formation. The knowledge obtained from this co-catalyst structure identification will be useful in elucidating the charge transfer mechanism, which is a critical factor determining photocatalytic activity in water splitting.

Acknowledgments

This research is supported by the National Science Council of Taiwan (NSC98-2221-E-006-110-MY3, NSC98-2622-E-006-012-CC2, NSC98-3114-E-007-011, NSC98-3114-E-007-005, and NSC98-2221-E-006-112-MY2) and the Bureau of Energy, Ministry of Economic Affairs, Taiwan (98-D0204-2). We also thank Mrs. Liang-Chu Wang of the Joint Center for High-Valued Instruments at the National Sun Yat-Sen University for her help in the HRTEM analysis.

References

[1] R.M.N. Yerga, M.C.A. Galvan, F. Del Valle, J.A. de la Mano, J.L.G. Fierro, ChemSusChem 2 (2009) 471.
[2] A. Kudo, Y. Miseki, Chem. Soc. Rev. 38 (2009) 253.
[3] A. Galinska, J. Walendziewski, Energy Fuels 19 (2005) 1143.
[4] J.C. Escudero, S. Cervera-March, J. Gimenez, R. Simarro, J. Catal. 123 (1990) 319.
[5] R. Niishiro, H. Kato, A. Kudo, Phys. Chem. Chem. Phys. 7 (2005) 2241.
[6] Z. Zou, J. Ye, K. Sayama, H. Arakawa, Nature 414 (2001) 625.
[7] A. Kudo, H. Kato, S. Nakagawa, J. Phys. Chem. B 104 (2000) 571.
[8] K. Shimizu, S. Itoh, T. Hatamachi, T. Kodama, M. Sato, K. Toda, Chem. Mater. 17 (2005) 5161.
[9] H.Y. Lin, T.H. Lee, C.Y. Sie, Int. J. Hydrogen Energy 33 (2008) 4055.
[10] H. Kato, A. Kudo, Catal. Lett. 58 (1999) 153.
[11] A. Kudo, H. Kato, Chem. Phys. Lett. 331 (2000) 373.
[12] H. Kato, A. Kudo, J. Phys. Chem. B 105 (2001) 4285.
[13] H. Kato, K. Asakura, A. Kudo, J. Am. Chem. Soc. 125 (2003) 3082.
[14] A. Iwase, H. Kato, H. Okutomi, A. Kudo, Chem. Lett. 33 (2004) 1260.
[15] Y. He, Y. Zhu, N. Wu, J. Solid State Chem. 177 (2004) 3868.
[16] D.G. Prob, P.A. Maggard, J. Solid State Chem. 179 (2006) 1727.
[17] W.H. Lin, C. Cheng, C.C. Hu, H. Teng, Appl. Phys. Lett. 89 (2006) 211904.
[18] C.C. Hu, H. Teng, Appl. Catal. A 331 (2007) 44.
[19] Y. Lee, T. Watanabe, T. Takata, M. Hara, M. Yoshimura, K. Domen, Bull. Chem. Soc. Jpn. 80 (2008) 423.
[20] J.W. Liu, G. Chen, Z.H. Li, Z.G. Zhang, Int. J. Hydrogen Energy 32 (2007) 2269.
[21] M. Choi, F. Oba, I. Tanaka, Phys. Rev. B 78 (2008) 014115.
[22] J.M. Lehn, J.P. Sauvage, R. Ziessel, Nouv. J. Chim. 4 (1980) 623.
[23] Z.G. Yi, J.H. Ye, Appl. Phys. Lett. 91 (2007) 254108.
[24] Z.G. Li, Y.X. Wang, J.W. Liu, G. Chen, Y.X. Li, C. Zhou, Int. J. Hydrogen Energy 34 (2009) 147.
[25] A. Iwase, H. Kato, A. Kudo, Catal. Lett. 108 (2006) 7.
[26] M. Higashi, R. Abe, A. Ishikawa, T. Takata, B. Ohtani, K. Domen, Chem. Lett. 37 (2008) 138.
[27] X. Zong, H. Yan, G. Wu, G. Ma, F. Wen, L. Wang, C. Li, J. Am. Chem. Soc. 130 (2008) 7176.
[28] J. Choi, S.Y. Ryu, W. Balcerski, T.K. Lee, M.R. Hoffmann, J. Mater. Chem. 18 (2008) 2371.
[29] K. Domen, S. Naito, T. Onishi, K. Tamaru, Chem. Phys. Lett. 92 (1982) 433.
[30] K. Domen, A. Kudo, T. Ohnishi, J. Catal. 102 (1986) 92.
[31] A. Kudo, A. Tanaka, K. Domen, T. Onishi, J. Catal. 111 (1988) 296.
[32] R.K. Selvan, V. Krishnan, C.O. Augustin, H. Bertagnolli, C.S. Kim, A. Gedanken, Chem. Mater. 20 (2008) 429.
[33] A.R. West, Basic Solid State Chemistry, 2nd ed., Wiley, New York, 1999. p. 319.
[34] K. Klier, K. Kuchynka, J. Catal. 6 (1966) 62.
[35] A. Bielański, M. Najbar, J. Catal. 25 (1972) 398.
[36] M. Breysse, B. Claudel, L. Faure, M. Guenin, R.J.J. Williams, J. Catal. 45 (1976) 137.
[37] A. Bielański, J. Haber, Catal. Rev. 19 (1979) 1.
[38] D.W. Hwang, H.G. Kim, J. Kim, K.Y. Cha, Y.G. Kim, J.S. Lee, J. Catal. 193 (2000) 40.
[39] K. Domen, A. Kudo, T. Onishi, N. Kosugi, H. Kuroda, J. Phys. Chem. 90 (1986) 292.
[40] C.C. Hu, C.C. Tsai, H. Teng, J. Am. Ceram. Soc. 92 (2009) 460.
[41] J.J. Zou, C.J. Liu, Y.P. Zhang, Langmuir 22 (2006) 2334.
[42] W. Choi, A. Termin, M.R. Hoffmann, J. Phys. Chem. 98 (1994) 13669.
[43] R.W. Cairns, E. Ott, J. Am. Chem. Soc. 55 (1933) 527.
[44] D.G. Barton, M. Shtein, R.D. Wilson, S.L. Soled, E. Iglesia, J. Phys. Chem. B 103 (1999) 630.
[45] C.J. Yang, J. Park, Y.R. Cho, Adv. Eng. Mater. 9 (2007) 88.
[46] J. Disdier, J. Herrmann, P. Pichat, J. Chem. Soc. Faraday Trans. 79 (1983) 651.
[47] A. Furube, T. Asahi, H. Masuhara, H. Yamashita, M. Anpo, Chem. Phys. Lett. 336 (2001) 424.
[48] K.E. Karakitsou, X.E. Verykios, J. Phys. Chem. 97 (1993) 1184.
[49] B.G. Streetman, S. Banerjee, Solid State Electronic Devices, fifth ed., Prentice Hall, Upper Saddle River, NJ, 2000, p. 142 (Chapter 5).
[50] D. Wang, Z. Zou, J. Ye, Chem. Mater. 17 (2005) 3255.
[51] A. Di Paola, E. García-López, S. Ikeda, G. Marcì, B. Ohtani, L. Palmisano, Catal. Today 75 (2002) 87.
[52] A. Di Paola, E. García-López, G. Marcì, C. Martin, L. Palmisano, V. Rives, A.M. Venezia, Appl. Catal. B 48 (2004) 223.
[53] M. Bellardita, M. Addamo, A. Di Paola, L. Palmisano, Chem. Phys. 339 (2007) 94.